Modeling of Casting, Welding and Advanced Solidification Processes - XI
Edited by Charles-André Gandin and Michel Bellet
TMS (The Minerals, Metals & Materials Society), 2006

PHASE FIELD THEORY OF LIQUID PHASE SEPARATION AND SOLIDIFICATION WITH MELT FLOW

György Tegze, László Gránásy

Research Institute for Solid State Physics and Optics; H-1525 Budapest, POB 49, Hungary

Keywords: Phase field theory, phase separation, solidification, melt flow, monotectic alloys

Abstract

A phase-field theory of binary liquid phase separation and solidification coupled to fluid flow is presented. The respective equations of motion and Navier-Stokes equations are solved numerically. We incorporate composition and temperature dependent capillary forces. The free energies of the bulk liquid phases are taken from the regular solution model. In the simulations, we observe Marangoni motion of the droplets, and direct and indirect hydrodynamic interactions between the droplets. We observe that capillary effects dramatically accelerate droplet coagulation and that solidification interacts with liquid phase separation.

Introduction

Phase separation in stable or metastable fluid phase miscibility gap may influence solidification considerably [1,2]. Such phenomena play an important role in various technological processes, including crystallization of proteins [1,2], polymers [3], and peritectic/monotectic systems [4]. For example, phase separation in metastable fluids and in glasses is known to assist the nucleation of the crystalline phase [1-4,5]. Two-phase alloys produced by freezing phase separating monotectic liquids are extensively used as self-lubricating bearing materials in automotive industry [4]. Efforts have been made to prepare structured monotectic textures via carefully controlling solidification [6]. The quality of the final products is determined by the microstructure of this type of alloys, which, in turn, is largely determined by complex phenomena taking place when the homogeneous liquid existing above the bimodal line is cooled through the two-phase region (see e.g., [1-6]). Therefore, a detailed understanding of these phenomena is of both theoretical and practical importance.

In these systems, solidification interacts with fluid phase separation, which in turn is a very complex phenomenon on its own: A broad variety of phenomena has been identified that influence the droplet dispersion during liquid phase separation as briefly reviewed in a recent paper [7]. In particular:

<u>Diffusion Controlled Processes</u>

(i) Coagulation due to Brownian motion of the droplets (Binder-Stauffer (BS) mechanism);
(ii) Evaporation-condensation type interaction (Lifshitz-Slyozov-Wagner (LSW) mechanism;
(iii) Diffusion coupling, where the iso-concentration lines include two or more droplets, which then attract or repulse each other depending on the composition gradient (Tanaka's first (T1) mechanism) [8];

<u>Hydrodynamic Effects</u>

(iv) Flow-assisted coagulation (FA);

(v) Collision-induced collision, where the flow field of two coagulating droplets induces further coagulation events (Tanaka's second (T2) mechanism) [9].
(vi) Hydrodynamic coarsening driven by capillary instability (Siggia's (S) mechanism) relevant for bicontinuous phase separation [10];

Hydrodynamic Effects Coupled to External Flow

(vii) Marangoni motion (M): Thermocapillary forces drive the droplets with a velocity increasing with size, thus large droplets capture smaller droplets.
(viii) Stokes motion (St): Buoyancy forces drive the droplets with a velocity increasing with the square of the linear size, thus large droplets capture smaller droplets.

Herein, we present a phase field theory of liquid phase separation and solidification in the presence of viscous flow that incorporates most of these mechanisms, an extension of our model used to describe liquid phase separation in the absence of solidification [6]. In this work, we concentrate on simultaneous solidification and liquid phase separation in the absence of gravity. We compute the time evolution of the size distribution of droplets and discuss the roles the individual processes may play in shaping the droplet distribution and solidification morphology.

Phase Field Theory of Polycrystalline Solidification with Fluid Flow

Our starting point is the polycrystalline phase field theory by Gránásy *et al.* [11] (that extends previous work by Kobayashi *et al.* [12]). It is combined here with melt flow as described by Anderson *et al.* [13] and Nestler *et al.* [14]. In our approach, the local state of the matter is characterized by the phase field, ϕ. This order parameter describes the extent of structural change during freezing and melting. The other basic field variables are the chemical composition c and the normalized orientation field θ [11]. The latter specifies the orientation of crystal planes in the laboratory frame. The free energy F consists of various contributions:

$$F = \int d^3r \left\{ \frac{\varepsilon_\phi^2 T}{2} \Gamma^2(\nabla\phi) + \frac{\varepsilon_c^2}{2}(\nabla c)^2 + f(\phi, c, |\nabla\theta|, T) \right\}, \tag{1}$$

where ε_ϕ and ε_c are constants, T is the temperature and $\Gamma(\nabla\phi) = s(\vartheta,\theta)|\nabla\phi|$, while $s = 1 + s_0\cos[k(\vartheta - 2\pi\theta/k)]$, and $\vartheta = \mathrm{atan}[(\nabla\phi)_y/(\nabla\phi)_x]$ is the orientation of the phase field interface. Here k is the symmetry index. (For four-fold symmetry, $k = 4$.) The Γ^2 term leads to a diffuse crystal-liquid interface, a feature observed both in experiment and computer simulations. The local free energy density is assumed to have the form $f(\phi,c,|\nabla\theta|,T) = w(\phi)Tg(\phi) + [1 - p(\phi)]\, f_S(c,T) + f_{ori}(|\nabla\theta|) + p(\phi)f_L(c,T)$, where the "double well" and "interpolation" functions have the forms $g(\phi) = {}^1/_4\,\phi^2(1-\phi)^2$ and $p(\phi) = \phi^3(10 - 15\phi + 6\phi^2)$, respectively, while the free energy scale $w(\phi) = (1 - c)\, w_A + c\, w_B$. The free energy surface has minima at $\phi = 0$ and $\phi = 1$ (corresponding to the crystalline and liquid phases), whose relative depth is the driving force for crystallization and is a function of both temperature and composition as specified by the free energy densities in the bulk solid and liquid, $f_{S,L}(c,T)$. Model parameters ε_ϕ, w_A, w_B, and ε_c are related to the free energy and thickness of the solid-liquid and liquid-liquid interfaces. To penalize spatial changes in the crystal orientation, in particular the grain boundaries, we introduce an orientational contribution f_{ori} to the free energy, which is invariant to rotations of the whole system:

$$f_{ori} = HT[1 - p(\phi)]\,|\nabla\theta|\,. \tag{2}$$

HT determines the magnitude of grain boundary energy. This specific choice ensures a narrow grain boundary, and successfully describes polycrystalline solidification and grain boundary dy-

namics [15]. The *local crystallographic* orientation is specified by the orientation field, $\theta \in [0, 1]$, which is a normalized orientation angle, related to the angle $\Xi = (2\pi/k)(\theta - \frac{1}{2}) \in [-\pi/k, \pi/k]$ measured relative to one of the axes of the (Cartesian) laboratory frame.

Time evolution is governed by relaxational dynamics, and Langevin noise terms (ζ_i) are added to model thermal fluctuations (essentially Langevin type equations, based on the time dependent Ginzburg-Landau formalism). The usual equations of motion are supplemented with appropriate convection terms. The second and third terms on the left hand side of the third equation couple the orientation and flow fields.

$$\frac{\partial \phi}{\partial t} + (\vec{v} \cdot \nabla)\phi = M_\phi \left\{ \nabla \left(\frac{\partial I}{\partial \nabla \phi} \right) - \frac{\partial I}{\partial \phi} \right\} + \zeta_\phi \,, \tag{3a}$$

$$\frac{\partial c}{\partial t} + (\vec{v} \cdot \nabla)c = \nabla \left\{ \frac{v_m}{RT} Dc(1-c) \nabla \left[\nabla \left(\frac{\partial I}{\partial \nabla \phi} \right) - \frac{\partial I}{\partial \phi} \right] + \zeta_j \right\}, \tag{3b}$$

$$\frac{\partial \theta}{\partial t} + (\vec{v} \cdot \nabla)\theta - A(\nabla \times \vec{v}) = M_\theta \left\{ \nabla \left(\frac{\partial I}{\partial \nabla \theta} \right) - \frac{\partial I}{\partial \theta} \right\} + \zeta_\theta \,, \tag{3c}$$

where I is the integrand in Equation 1 (plus the term with the Lagrange multiplier ensuring conservation of field c), while $A = k/4\pi$. The time scales for the three fields are determined by the appropriate coarse-grained mobilities M_ϕ, M_c and M_θ that appear in the equations of motion. These coarse-grained mobilities may be taken from experiments and/or evaluated from atomistic simulations [16]. For example, the mobility M_c, is directly proportional to the classic interdiffusion coefficient for a binary mixture, the mobility M_ϕ dictates the rate of crystallization, while M_θ controls the rate at which regions reorient.

We assumed here an incompressible, viscous liquid, and that the mass density is independent of composition and phase. The mass and momentum balance are described by the equations

$$(\nabla \cdot \vec{v}) = 0 \,, \tag{3d}$$

$$\rho \frac{\partial \vec{v}}{\partial t} + \rho(\vec{v} \cdot \nabla)\vec{v} = \rho \vec{g} + \nabla \cdot \mathbf{P} \,, \tag{3e}$$

respectively. Here ρ is the mass density, $\vec{v}$ the velocity, and $\rho \vec{g}$ is the gravitational force, while

$$\mathbf{P} = \mathbf{I} \left\{ -P + \varepsilon_c^2 \left[\frac{1}{2}(\nabla c)^2 + c\nabla^2 c \right] + \frac{1}{2}\varepsilon_\phi^2 T \Gamma^2 \right\} - \varepsilon_c^2 (\nabla c \otimes \nabla c) - \varepsilon_\phi^2 T \Gamma (\vec{\xi} \otimes \nabla \phi) - [1 - p(\phi)] HT \left(\frac{\nabla \theta}{|\nabla \theta|} \otimes \nabla \theta \right) + \mathbf{\Pi} \tag{3f}$$

is a generalization of the usual non-classical stress tensor [13,14]. The latter is divided into a non-dissipative part (that includes the capillary terms emerging from spatial variation of the fields ϕ, c, and θ) and into a dissipative part represented by the viscous stress tensor, $\mathbf{\Pi}$. ($\mathbf{I}$ is the unit tensor, $\otimes$ stands for diadic product, while $\vec{\xi} = \partial \Gamma / \partial(\nabla \phi)$.) Note that in our model solidification is represented by an increase in the viscosity, and that the term $-P$ incorporates the osmotic pressure $f - c(\partial f / \partial c)$.

Numerical Solution

The phase field, concentration, and orientation equations have been solved numerically on an equidistant rectangular grid using an explicit finite difference scheme. The hydrodynamic equations have been solved on a respective staggered grid by a semi-implicit mixed, finite volume – spectral scheme. This allows the use of "solid" viscosities that are up to 10^3 times larger than the

liquid viscosity. Rectangular grids of sizes 250 × 250, 500 × 500, and 1000 × 1000 were used. We applied periodic boundary conditions. The noise has been discretized as described by Karma and Rappel [17]. A parallel code has been developed and run on a PC clusters, consisting of 100 nodes of AMD Athlon 64 3200+ processors. The size distribution of the droplets has been evaluated from the chemical composition maps using the software ImageJ.

Physical Properties

The computations were performed with the physical properties of the Al-Bi system. The free energies have been obtained from the regular solution model, whose parameters were chosen so that the corresponding phase diagram (Figure 1) reflects the main features of the experimental one. The melting point, the heat of fusion and the (average) molar volume of the pure constituents were taken as T_A = 933.3 K, $H_{f,A}$ = 10.79 kJ/mol, T_B = 544.5 K, $H_{f,B}$ = 11.3 kJ/mol, v_m = 15.7 cm^3/mol, while the interaction parameter and its temperature coefficient were assumed to be Ω_S = 42 kJ/mol and $d\Omega_S/dT$ = 10 J/mol/K in the solid and Ω_L = 32 kJ/mol and $d\Omega_L/dT$ = 10 J/mol/K in the liquid, respectively. ε_c has been chosen so that the liquid-liquid surface tension γ = 60 mJ/m^2 [18] is recovered at the monotectic temperature. To enhance the thermo-capillary effects, we increased $d\gamma/dT$ by a factor of ~ 30. In the calculations for phase separation, unless stated otherwise, we fix the temperature to T = 902 K and set the initial chemical composition to c_0 = 0.25. This exceeds the monotectic temperature, therefore no solidification occurs, and falls into the spinodal regime. Thus the time scale of the processes is set by the interplay of melt flow and chemical diffusion. Accordingly, the equations are made dimensionless using the length and time scales of $\xi = 6\times10^{-6}$ cm, $\tau = \xi^2 / D = 1.2$ μs, where $D = 3\times10^{-5}$ cm^2/s is the diffusion coefficient. The dimensionless time and spatial steps were chosen as $\Delta t = 1.25\times10^{-7}$ and $\Delta x = 5\times10^{-3}$, ($\Delta t/3$ and $2\Delta x/3$, in the case of solidification). The upper limits of the time period and linear size of our simulations fall in the μs and μm range, respectively. A viscosity of 1 mPa.s was used in the liquid phases, while in the solid a 500 times larger value was taken.

Results and Discussion

Kinetics of Liquid Phase Separation

Here, we investigate the effect of all mechanisms described above, with the exception of

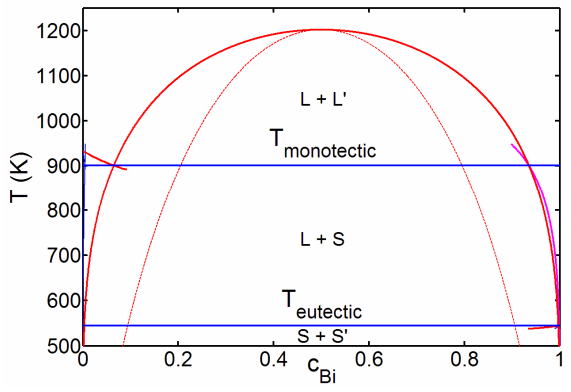

Figure 1. Phase diagram of the Al-Bi system calculated using the regular solution model. The liquid compositions for the two-phase equilibria (liquidus and liquid bimodal lines and their metastable continuations) are denoted by heavy lines, while the thin line stands for the liquid spinodal. The temperatures for three-phase equlibria (monotectic and eutectic temperatures) are denoted by heavy horizontal lines.

Brownian motion (BS) and the gravity-driven (St) coagulation of the droplets. In agreement with a large number of studies, in the *diffusion-based* LSW process the larger droplet grows on the expense of the smaller one (not shown here). Symmetric droplets without melt flow coagulate via the *diffusion-controlled* T1 mechanism. The effect of melt flow on coagulation is visualized by image sequences Figures 2(a)-(b) and (a),(c)-(f). In the absence of flow, the rate-limiting factor is chemical diffusion, and coagulation happens on the diffusive time scale. The presence of melt flow dramatically accelerates the merging the two droplets. The final droplet formed by coagulation performs oscillations that are damped in time by viscous dissipation. This flow assisted (FA) coagulation of droplets is orders of magnitude faster than the purely diffusive T1 mechanism. These findings are in accord with results on transparent organic liquids [8].

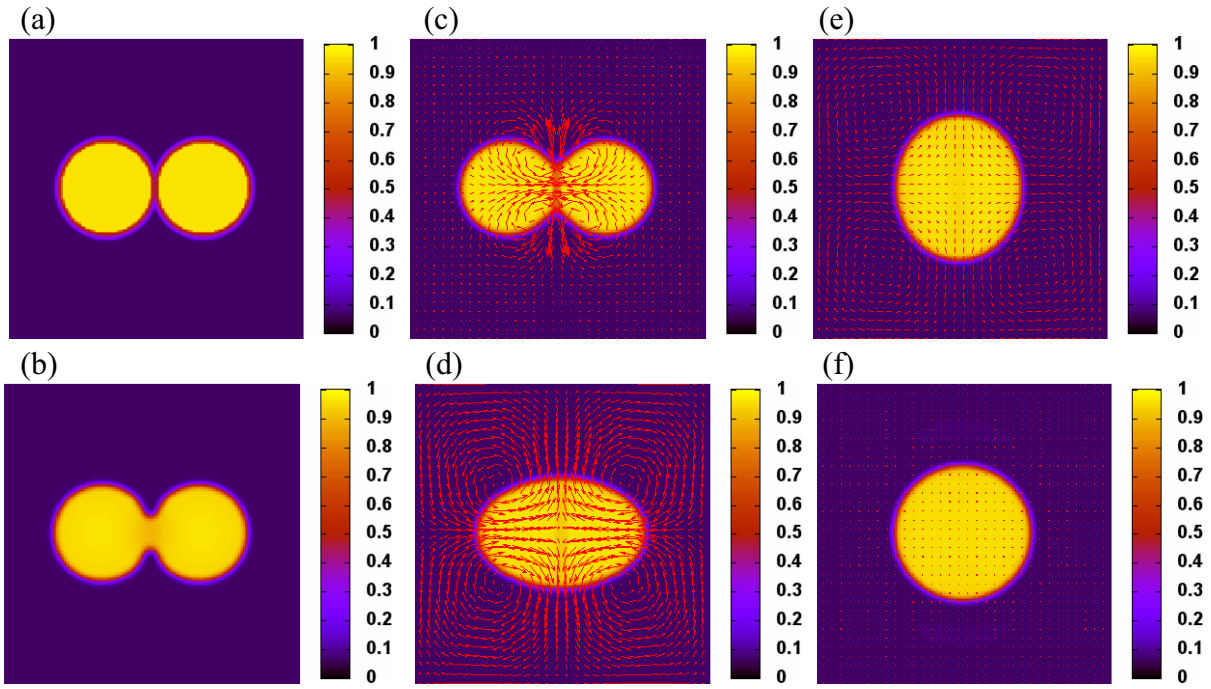

Figure 2. Coarsening mechanisms for two droplets (a),(b) Diffusion controlled coagulation (T1). Snapshots taken at (a) 0 and (b) 2.5×10^{-2} dimensionless times. (a),(c)-(f) Flow assisted (FA) coagulation. Upper and lower parts are from snapshots taken at 0, 1.25×10^{-4}, 1×10^{-3}, 2×10^{-3} and 5×10^{-3} dimensionless times. The arrows indicate the velocity field. Composition maps are shown. The colorbars show the relation between Bi concentration and hues. Note the sluggishness of the purely diffusive processes T1, the strong outward flow building up along the vertical axis between the two collapsing drops, and the weak inward flow along their horizontal axis. (Computed on a 200×200 grid.)

Complex hydrodynamic interactions occur in the presence of several droplets. As found by Tanaka [9], the flow field generated by two coagulating droplets "sucks" closer the droplets at the far ends of the two coagulating droplets, while it "pushes" them farther on the elongated sides. When the droplet density is high, these motions often induce further coagulation events (mechanism T2). We observe such chains of coagulation events in our simulations (Figure 3).

Results on Marangoni motion (M) of Bi rich liquid droplets in an Al rich liquid in a constant temperature gradient is shown in Figure 4. Panels (a) and (b) compare the flow fields developing inside the droplets in the laboratory frame and in a coordinate system fixed to the geometrical center of the droplet. In agreement with analytical predictions [19], we find that the steady state velocity increases with increasing droplet diameter (Figure 4(c)). The growth rate increases both

with the temperature gradient, and with the temperature coefficient of the surface tension, as follows from analytical theory [19].

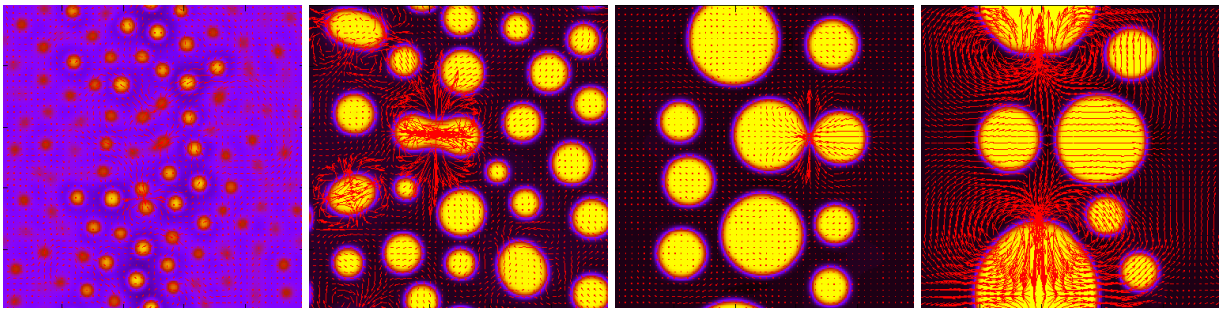

Figure 3. Hydrodynamic interaction of several droplets at various stages of liquid phase separation in an Al-Bi alloy of c = 0.25 at. % Bi content, at 920 K. The temperature increases linearly towards the vertical centerline on both sides. This induces Marangoni motion towards the center from both sides. Simulations were performed on a 500×500 grid. Note the flow field of the coagulating droplet pairs: Outward flow at their "neck", inward flow along the longer axis.

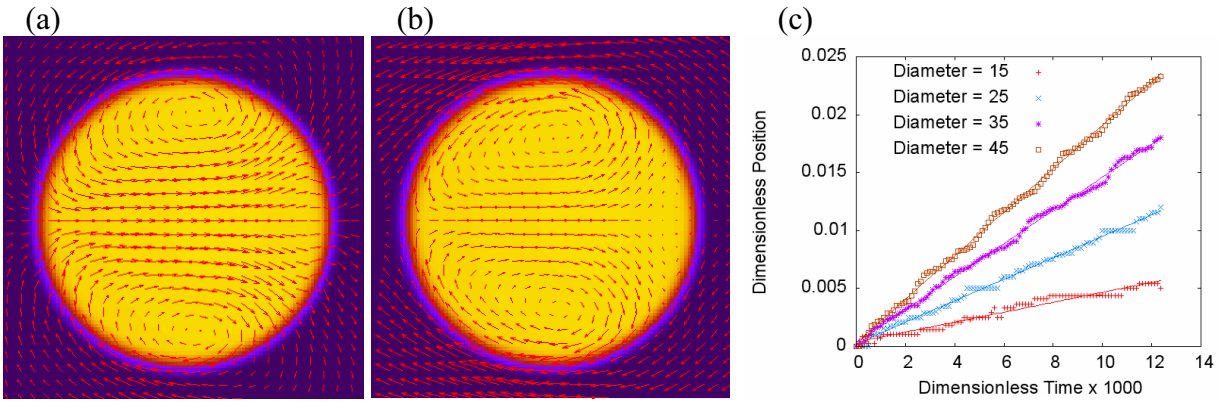

Figure 4. Marangoni motion as predicted by the phase field theory. The flow field and the concentration map of a 24 nm droplet are shown: (a) The velocity field in the laboratory frame, and (b) the velocity field in the coordinate system fixed to the geometrical center of the droplet. (c) Droplet position as a function of time. Lines are to guide the eyes. The simulations were performed on a 250×250 grid. Temperature increases from left to the right.

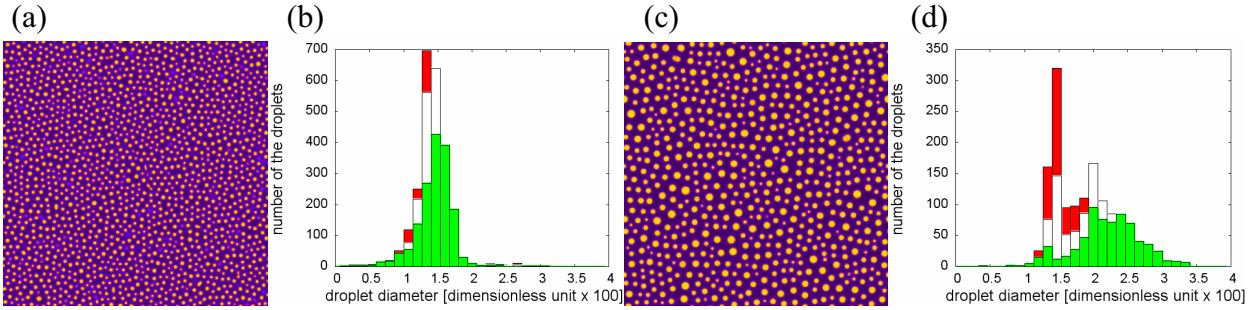

Figure 5. Liquid phase separation in Al-Bi as predicted by the phase field theory: (a),(b) Without melt flow and (c),(d) with melt flow. Snapshots of the concentration fields ((a),(c)) taken at dimensionless time 0.051 are shown. Histograms showing the respective droplet size distributions

at three dimensionless times (0.025, 0.031, and 0.051) for the two cases are presented in panels (b) and (c).

Droplet Size Distributions

We investigate the effect of the hydrodynamic flow and thermo-capillary forces on the droplet size distribution on a grid of size 1000 × 1000. Two cases are compared: (a) Purely diffusive interaction and (b) diffusive and hydrodynamic interactions. The respective images and droplet size distributions are shown in Figure 5. Flow significantly accelerates liquid phase separation.

Solidification of Phase Separating Liquid

Simulations have been performed for $c = 0.1$ at $T = 700$ K (above the eutectic temperature, where partial solidification is possible). Solid layers have been placed on the left and right sides of the simulation window. The time evolution of the system is displayed in Figure 6. It appears that the solute pile up ahead of the advancing solidification front enhances locally the rate of phase separation, a process of oscillatory nature, which yields quasi-periodically frozen-in droplet lines parallel to the growth front. This mechanism seems to dominate the distribution of frozen-in droplets rather than phase separation morphology in the liquid. Work is underway to study the importance of this mode of droplet formation under practical conditions.

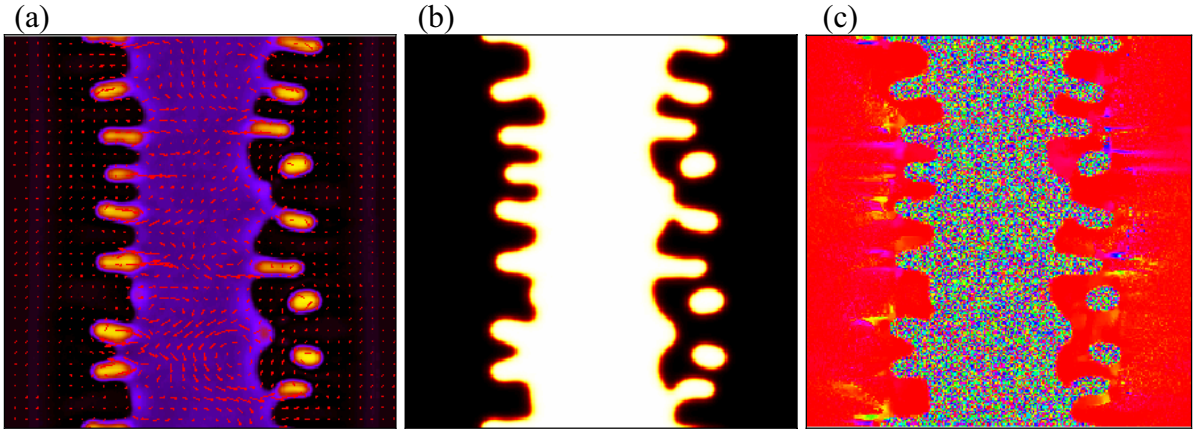

Figure 6. Phase separation in the presence of advancing solidification fronts in an Al-Bi alloy of $c_0 = 0.1$ Bi content between 800 K (sides) and 900 K (vertical centerline). Snapshots of the (a) composition (dark hue is the solid), (b) phase field (dark is the solid phase) and (c) orientation fields are shown. The simulation has been performed on a 250×250 grid. Note the interface induced formation of Bi droplets and the appearance of new orientations in the solid. The arrows indicate an essentially random flow.

Summary

We presented a phase field model of phase separation and solidification in monotectic liquids. Our simulations show that flow significantly accelerates liquid phase separation and that interaction between solidification and phase separation may influence the droplet size distribution.

Acknowledgments

The authors thank M. Conti and M. Tegze for the enlightening discussions. This work has been supported by contracts OTKA-T-037323 and ESA PECS No. 98021, and forms part of the ESA MAP Projects No. AO-99-026 "MONOPHAS".

References

1. D. Rosenbaum, P.C. Zamora, and C.F. Zukoski, "Phase Behavior of Small Attractive Colloidal Particles," *Phys Rev Lett*, 76 (1) (1996), 150-153.

2. P.R. ten Wolde and D. Frenkel, "Enhancement of Protein Crystal Nucleation by Critical Density Fluctuations," *Science*, 277 (5334) (1997), 1975-1978.

3. A. Keller and S.Z.D. Cheng, "The Role of Metastability in Polymer Phase Transitions," *Polymer*, 39 (19) (1998), 4461-4487.

4. L. Ratke and S. Dieffenbach, "Liquid Immiscible Alloys," *Mater Sci Eng R,* 15 (1995), 263-347.

5. A.H. Ramsden and P.F. James, "The Effects of Amorphous Phase Separation on Crystal Nucleation Kinetics in BaO-SiO_2 Glasses. 1. Genaral Survey," *J Mater Sci*, 19 (5) (1984), 1406-1419.

6. H. Yasuda et al., "Fabrication of Porous Aluminium with Deep Pores by using Al-In Monotectic Solidification and Electrochemical Etching," *Mater Lett*, 58 (6) (2004), 911-915.

7. G. Tegze, T. Pusztai, and L. Gránásy, "Phase Field Simulation of Liquid Phase Separation with Fluid Flow," *Mater Sci Eng A*, 413-414 (2005) 418-422.

8. H. Tanaka, "A New Coarsening Mechanism of Droplet Spinodal Decomposition," *J Chem Phys*, 103 (6) (1995), 2361-2364.

9. H. Tanaka, "Coarsening mechanisms of Droplet Spinodal Decomposition in Binary Fluid Mixtures," *J Chem Phys*, 105 (22) (1996), 10099-10114.

10. E.D. Siggia, "Late Stages of Spinodal Decomposition in Binary Mixtures," *Phys Rev A*, 20 (2) (1979), 595-605.

11. L. Gránásy, T. Börzsönyi, and T. Pusztai, "Nucleation and Bulk Crystallization in Binary Phase Field Theory," *Phys Rev Lett*, 88 (20) (2002), 206105-1-4.

12. R. Kobayashi, J.A. Warren, and W.C. Carter, "Vector-Valued Phase Field Model for Crystallization and Grain Boundary Formation," *Physica D*, 119 (3-4) (1998), 415-423.

13. D.M. Anderson, G.B. McFadden, and A.A. Wheeler, "A Phase-Field Model of Solidification with Convection," *Physica D*, 135 (1-2) (2000), 175-194.

14. B. Nestler et al., "Phase-Field Model for Solidification of a Monotectic Alloy with Convection," *Physica D*, 141 (1-2) (2000), 133-154.

15. J.A. Warren et al., "Extending Phase Field Models of Solidification to Polycrystalline Materials," *Acta Mater*, 51 (20) (2003), 6035-6058.

16. J.J. Hoyt, M. Asta, and A. Karma, "Atomistic and Continuum Modeling of Dendritic Solidification," *Mater Sci Eng R*, 41 (6) (2003), 121-163.

17. A. Karma and W.-J. Rappel, "Phase-Field Model of Dendritic Sidebranching with Thermal Noise," *Phys Rev E*, 60 (4) (1999), 3614-3625.

18. W. Hoyer, I. Kaban, and M. Merkwitz, "Liquid-Liquid Interfacial Tension in Immiscible Binary Al-Based Alloys," *J Optoelectr Adv Mater*, 5 (5) (2003), 1069-1073.

19. L. Ratke and W.K. Thieringer, "The Influence of Particle Motion on Ostwald Ripening in Liquids," *Acta Metall*, 33 (10) (1985), 1793-1802.